Analytica Chimica Acta 1232 (2022) 340447

Contents lists available at ScienceDirect

Analytica Chimica Acta

journal homepage: www.elsevier.com/locate/aca

A machine learning-based multimodal electrochemical analytical device based on eMoS$_x$-LIG for multiplexed detection of tyrosine and uric acid in sweat and saliva

Vinay Kammarchedu [a,b,c], Derrick Butler [a,b,c], Aida Ebrahimi [a,b,c,d,*]

[a] Department of Electrical Engineering, The Pennsylvania State University, University Park, PA, 16802, United States
[b] Center for Atomically Thin Multifunctional Coatings, The Pennsylvania State University, University Park, PA, 16802, United States
[c] Materials Research Institute, The Pennsylvania State University, University Park, PA, 16802, United States
[d] Department of Biomedical Engineering, The Pennsylvania State University, University Park, PA, 16802, United States

HIGHLIGHTS

- Multiplexed sensing of tyrosine and uric acid is achieved using machine learning-powered electrochemical eMoS$_x$-LIG sensors.
- Compared to bare LIG, eMoS$_x$-LIG shows 3× higher ECSA and 1.5× higher heterogenous electron transfer rate.
- Combining ML with multimodal electrochemical sensing enables accurate quantification of analytes in mixtures.
- Using the optimized ML architecture, a limit of detection 100× better than conventional methods is obtained.
- On-body sweat analysis is shown using the flexible sensor over a wide concentration range covering the physiological window.

GRAPHICAL ABSTRACT

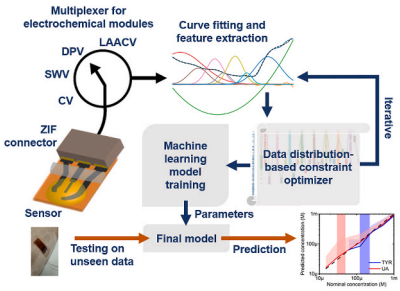

ARTICLE INFO

Keywords:
Multiplexed biosensor
Multimodal sensing
Machine learning
Laser induced graphene
Sweat
Saliva
Wearable

ABSTRACT

Multiplexed detection of biomolecules is of great value in various fields, from disease diagnosis to food safety and environmental monitoring. However, accurate and multiplexed analyte detection is challenging to achieve in mixtures using a single device/material. In this paper, we demonstrate a machine learning (ML)-powered multimodal analytical device based on a single sensing material made of electrodeposited molybdenum polysulfide (eMoS$_x$) on laser induced graphene (LIG) for multiplexed detection of tyrosine (TYR) and uric acid (UA) in sweat and saliva. Electrodeposition of MoS$_x$ shows an increased electrochemically active surface area (ECSA) and heterogeneous electron transfer rate constant, k^0. Features are extracted from the electrochemical data in order to train ML models to predict the analyte concentration in the sample (both singly spiked and mixed samples). Different ML architectures are explored to optimize the sensing performance. The optimized ML-based multimodal analytical system offers a limit of detection (LOD) that is two orders of magnitude better than

Abbreviations: LIG, Laser induced graphene; ML, Machine learning; TYR, Tyrosine; UA, Uric acid; eMoS$_x$, Electrodeposited molybdenum polysulfide; LOD, Limit of detection; ECSA, Electrochemically active surface area.

* Corresponding author. Department of Electrical Engineering, The Pennsylvania State University, University Park, PA, 16802, United States.
E-mail address: sue66@psu.edu (A. Ebrahimi).

https://doi.org/10.1016/j.aca.2022.340447
Received 31 May 2022; Received in revised form 19 September 2022; Accepted 23 September 2022
Available online 29 September 2022

conventional approaches which rely on single peak analysis. A flexible and wearable sensor patch is also fabricated and validated on-body, achieving detection of UA and TYR in sweat over a wide concentration range. While the performance of the developed approach is demonstrated for detecting TYR and UA using eMoS$_x$-LIG sensors, it is a general analytical methodology and can be extended to a variety of electrochemical sensors to enable accurate, reliable, and multiplexed sensing.

1. Introduction

The accuracy and reliability of diagnostics can be improved by simultaneous analysis of multiple biomarkers using multiplexed methods [1]. In addition, multiplexed detection within the same sample saves resources and reagents, which is critical with clinical samples that often have limited volume [2]. Conventionally, multiplexing is achieved by various approaches, such as the use of different capture molecules (as in multiplexed enzyme linked immunosorbent assay (ELISA) [3]) or using spectroscopic methods, such as surface enhanced Raman spectroscopy (SERS), mass spectrometry [4], and high performance liquid chromatography [5]. While spectroscopic methods are inherently multiplexed [6], they are more suited for lab-based analysis as they often require bulky and expensive equipment [7].

Electrochemical sensors have emerged as the hallmark of point of care (POC) and wearable technology, as they can sensitively monitor analytes and are portable, relatively low-cost, and compatible with IC technology for integration with signal processing and data transmission modules [8]. In particular, electrochemical sensors have found ever-growing interest for detection and monitoring redox-active small molecules, such as catecholamines and their metabolites [9–12], reactive oxygen species (ROS) [13,14], reactive nitrogen species [15], among others. Various electrochemical methods have been utilized, including cyclic voltammetry (CV) [16,17], square wave voltammetry (SWV) [18,19], differential pulse voltammetry (DPV) [20,21], and large amplitude AC voltammetry (LAACV) [22,23]. However, when the formal potential of molecules is close, there is a considerable overlap between their redox peaks and therefore it is more challenging to distinguish them in mixed samples. To achieve reliable and multiplexed sensing and mitigate stability issues caused by device-to-device variations, machine learning (ML) offers a powerful tool [24,25]. For example, ML-based support vector machine (SVM) models have been used to estimate nitrate concentration in water sources using CV [26]. In other works [27,28], fast scan cyclic voltammetry (FSCV) is used along with ML to accurately predict the dopamine and serotonin levels in extracellular brain fluid. ML has also been used to selectively detect heavy metal ions in buffer solutions in the presence of interferents [29]. Convergence of ML and multimodal electrochemical readout to create fingerprint of analytes can help achieve multiplexing with high accuracy [22]. However, ML-assisted electrochemical biosensing is still in inceptive stage [24,31].

In this work, we demonstrate a ML-powered multimodal analytical device based on electrodeposited molybdenum polysulfide (eMoS$_x$) on laser induced graphene (LIG) for multiplexed detection of tyrosine (TYR) and uric acid (UA) in sweat and saliva samples. To enable automated multimodal readout, a customized electrochemical data collection setup is developed which automatically sweeps through multiple electrochemical modalities. The developed platform enables automated background subtraction and peak identification which filters the background signals before being passed to the ML model for regression in order to detect TYR and UA in mixed samples. TYR is a precursor for production of catecholamine neurochemicals [32], and under stress, its level decreases [33]. Abnormal levels of UA is indicative of kidney failure [34]. High concentration of UA leads to gout [35] and other medical conditions, such as kidney stones, diabetes, and cardiovascular diseases [36]. Hence, detection and tracking the levels of TYR and UA is important for early disease diagnosis, prognosis, and treatment. TYR and UA are present in saliva and sweat in considerable quantities allowing for non-invasive testing, which is an essential criterion for routine preventive care and personalized medicine. Supplementary Information (SI, Section S2) summarizes some of the prior works reported for detecting TYR and/or UA, including a few recent reports based on LIG. In our work, compared to bare LIG, eMoS$_x$-functionalized LIG has a 300% larger electrochemically active surface area (ECSA) and a 50% larger standard heterogenous electron transfer rate constant (k^0), both of which lead to an improved sensitivity to TYR and UA. Using a custom-made automated hardware/software analytical system, several voltammetry methods (CV, SWV, DPV, LAACV) are investigated to study multimodal data fusion for enhancement of the analytical performance, which has not been previously studied in detail to the best of our knowledge. To analyze the multimodal data, the ML architecture is optimized, enabling selective and sensitive detection of TYR (LOD 100 *nM*) and UA (LOD 10 *nM*) in saliva and sweat at pH 6.7. Finally, on-body experiments demonstrate the application of the eMoS$_x$–LIG sensor as a wearable patch for sweat analysis. While the ML-based multimodal electrochemical analytical method is demonstrated using TYR and UA, the developed methodology can be extended to other sensory systems including environmental monitoring, food safety, biodefense, and molecular diagnostics.

2. Experimental details

2.1. Sensor fabrication and functionalization of laser induced graphene (LIG)

Commercially available polyimide sheets are rinsed with 2-propanol (IPA) followed by air drying to clean the surface and are mounted on the metal workbench in a commercial CO_2 laser cutter (VLS2.30, Universal Laser Systems, Inc.) using adhesive tapes at the edges of the polyimide sheet. A 25 *W* laser is used to ablate polyimide into conductive laser induced graphene (LIG) [37]. The laser writing parameters are optimized in order to get good conductivity and structural integrity [38]. The laser beam is focused onto the polyimide sheet and a power scaling of 10.5% with a speed scaling of 5.5% and a resolution of 1000 pixels per inch (ppi) in raster mode is used to directly write the sensor pattern onto the polyimide substrate.

The sensor has a three-electrode design with a working electrode (WE; eMoS$_x$-LIG), a counter electrode (CE; LIG), and a reference electrode (RE) configured with pads to be able to be inserted into a commercial zero insertion force (ZIF) connector as shown in Fig. 1. Commercial Ag/AgCl glass reference electrode (MF-2052, Bioanalytical Systems, Inc.) is used to characterize the sensors initially. For on-chip and on-body measurements, a pseudo reference electrode is fabricated by writing upon the LIG RE pattern using a conductive silver pen (Circuit Scribe).

LIG is functionalized with MoS$_x$ using electrodeposition, as shown in Fig. 1. Amperometric electrodeposition at $-0.8\ V$ in $1\ mg\ mL^{-1}$ ammonium tetra-thiomolybdate (ATTM) with $1\ mg\ mL^{-1}$ potassium chloride (KCl) as supporting electrolyte is used to deposit MoS$_x$ onto the WE with platinum CE and Ag/AgCl RE [39]. Silicone (Ecoflex 5, Smooth-On, Inc.) is used to passivate the sensor region from the electrical contact pads. The sensor pattern also has visual cues in the form of electrically disconnected LIG dots and lines to help consistent and repeatable application of the passivation layer on the surface. After fabrication, the sensors are either used immediately or stored in N_2 or dry environment (ambient) for three weeks to determine the shelf life.

2.2. Hardware and software setup

Commercially available potentiostat (MultiPalmsens, PalmSens) is used to perform the following standard voltammetry measurements: CV, SWV, and DPV. In order to perform LAACV [23], a custom hardware platform is built similar to our previously reported work [12]. The custom hardware is programmed to apply a sinusoid with frequency of 100 *Hz* and $V_{pk} = 100$ *mV* imposed upon a ramp waveform potential to the electrochemical cell and measure the current.

Since machine learning demands a large amount of data to be collected for training and testing the model, we also built a custom multiplexer sensor holder capable of handling multiple sensors at once, see schematic block diagram in Fig. S1 (SI, Section S3). This system is comprised of eight ZIF sensor receptacles with glass reference electrode mounts fabricated in commercial plexiglass sheets. Eight sensors are inserted at once into the connectors and the multiplexer is programmed to automatically route each sensor to a particular potentiostat: commercial potentiostat for standard electrochemical modules: CV, DPV, SWV and custom potentiostat for custom electrochemical module: LAACV.

A Python supported Jupyter Notebook is used as the software interface to connect to the multiplexer to control the relays and route the signals. A schematic of the software flow is shown in Fig. S2 (SI, Section S4). Briefly, the Jupyter notebook directly interfaces to the custom potentiostat using a serial port. A C# based wrapper is also written for the commercial potentiostat so that it also could be controlled by the Jupyter notebook. All the data collected is automatically stored onto the PC with appropriate time stamps and experimental conditions. Another Jupyter notebook running in a loop constantly searches for new data and immediately partially processes and plots the data in real time. Scikit-learn [40] was mainly used to implement the machine learning pipeline along with NumPy [41] and SciPy [42]. Default machine learning model parameters were used as is from the imported libraries unless specified. The machine learning model described later can analyze the data collected and predict the analyte concentrations in real time (<15 *secs* on a standard PC after the data is collected by the potentiostat). The computational cost depends upon the chosen complexity of the model and chosen electrochemical modules (ranges from < 3 *secs* to < 15 *secs*). The trained model can also be implemented on an embedded or a smartphone system allowing for mobile computation and prediction.

2.3. Electrochemical analyses

TYR and UA stock solutions with concentration of 1 *mM* are prepared in artificial saliva (AS) and artificial sweat (ASW). Other concentrations are prepared by serial dilution of the stock solutions in the corresponding medium. The stock solution is remade every week to prevent degradation (if any) which could affect the data repeatability. In order to test a sensor, it is first rinsed with DI water and then a baseline AS/ASW drop of 100 μL is added. Cyclic voltammetry is performed to condition the sensor (parameters in SI, Section S5) and ensure that the electrical contact to the sensor is reliable and not noisy (e.g. due to loose connections of the wiring and ZIF connectors). Then, baseline DPV, SWV, and LAACV signals (parameters in SI, Section S5) are collected. To test the analytes, the baseline liquid is wicked off (VWR, Spec-Wipe) and 100 *uL* of a given concentration is added one by one and DPV, SWV, LAACV data is collected making sure the concentration of the analyte always increases on that particular sensor to prevent back contamination and separate wicks are maintained to prevent cross contamination between the sensors. Three scans for each measurement module are obtained. To gauge the sensor response using the single peak analysis method described in Section 3.2, only the third scan is used. However, all scans are utilized to train the ML models described in Section 3.3. For all measurements, at least four sensor replicates are used.

For the sensor shelf-life tests, a separate stock solution is maintained with 1 *mM* TYR. Two set-pairs of sensors, four in each set is maintained to test the storage environment. One set stays in the ambient environment, whereas one set is stored in a N_2 desiccator. To test the sensor shelf-life, three set-pairs of sensors are prepared: three sets are stored in N_2 desiccator (<2*ppm* moisture) and three sets in ambient environment. A set from each environment is tested with a week gap using 250 *uM* TYR. For selectivity tests, all combinations of the two analyte mixture concentrations are tested in sequence as described above ensuring that no single sensor sees a decrease in concentration of a particular analyte being tested on it.

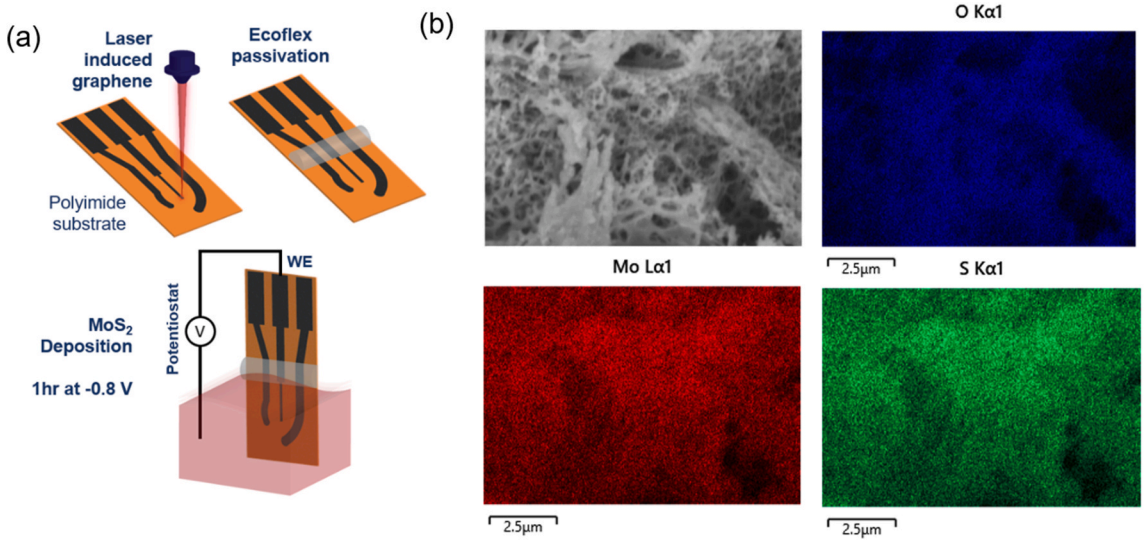

Fig. 1. Fabrication, functionalization, and material characterization of eMoS$_x$-LIG sensor. (a) First, polyimide is converted to laser induced graphene (LIG) using laser processing. Contact pads are passivated using silicone to define the working electrode (WE) area. Amorphous MoS$_x$ is electrodeposited using chronoamperometry method with the WE voltage set at −0.8 V vs. Ag/AgCl. (b) SEM image (top left) and EDX maps of eMoS$_x$-LIG confirm the 3D porous structure of the material and distribution of Mo, S, and O elements.

3. Results and discussion

3.1. Characterization of the material morphology, surface chemistry, and kinetic parameters

Scanning electron microscopy (SEM) reveals a fibrous and porous structure of LIG as shown in Fig. 1b. The porous structure leads to a significant increase of the available surface area, providing many active sites for electrochemical reactions [43]. Raman spectroscopy in Fig. S3 (SI, Section S6) confirms successful carbonization of the polyimide sheet and presence of graphite and graphene. Energy Dispersive X-ray spectroscopy (EDX) in Fig. 1b also confirms the presence of Mo, S, and O. X-Ray photoelectron spectroscopy (XPS) confirms successful electrodeposition of MoS_x on LIG as shown in Table S1 (SI, Section S6) [39]. Specifically, Mo to C ratio on the surface is observed to be ~1:6 among which 53% Mo is in MoS_2 and 15% Mo in MoO_2/MoS_3. Interestingly, considerable amount of the Mo (32%) is in MoO_3, which has also been reported previously [44] and has shown catalytic properties for oxidation reactions [45]. The amorphous MoS_x is shown to transition into a crystalline structure following high temperature annealing in inert gas [10]. Fig. S3c summarizes the XRD results. The XRD of LIG shows the (002) and (100) plane of the graphite-2H (PDF 41-1487), consistent with previous reports [46]. There is no obvious MoS_x characteristic peak found in the XRD results of the $eMoS_x$-LIG sample since the material in our study is amorphous (no post-deposition thermal annealing is performed), consistent with previous reports [47].

Brunauer-Emmett-Teller (BET) measurements were also carried out to estimate the surface area of the electrodes. The results are shown in Fig. S3d and summarized in Table S2. The BET-estimated surface area is similar to previously reported values for bare LIG [48]. It is found that electrodeposition of MoS_x increases the physical surface area by about 25%. It is also interesting to note that the pore volume of pores smaller than 13 Å was found to decrease nearly two times due to the MoS_x electrodeposition. As previous studies have shown, electrodeposition can greatly modify the surface morphology and hence the surface area of the material along with other mesoporous characteristics [49].

The CO_2 infrared laser ablates polyimide, which contains aromatic and repeated imide groups, and converts the sp^3-carbon atoms to sp^2-carbon atoms thus generating a three-dimensional (3D) and porous conductive graphite network [50]. The porous and 3D structure of LIG tremendously increases the surface area available for sensing applications. Table 1 summarizes the calculated electrochemically active surface area (ECSA) and the heterogenous electron transfer rate constant, k^0, for both LIG and $eMoS_x$-LIG. ECSA and k^0 of the LIG sensor (geometric area = 0.9 mm^2) are characterized using redox probes (5 mM Ferricyanide and Ferrocyanide) in Dulbecco's phosphate-buffered saline (DPBS) [38]. Cyclic voltammograms and their extracted features are shown in Figs. S4a and b. The linear fit and corresponding ECSA and k^0 are calculated from the data shown in Fig. S4 (SI, Section S7). The images correspond to the peak current and ψ (unitless potential) vs. the cyclic voltammetry scan rate, v. Randles-Sevcik equation is used to calculate the area as follows:

$$i_{peak} = 0.4463 n^{1.5} F^{1.5} C A \sqrt{\frac{Dv}{RT}} \quad \text{Eq. 1}$$

The heterogeneous electron transfer rate, k^0, is calculated using the following equation:

$$\psi = k^0 \sqrt{\frac{RT}{\pi D n F v}} = \frac{-0.6288 + 0.0021\left(\Delta E_{peak} n\right)}{1 - 0.017\left(\Delta E_{peak} n\right)} \quad \text{Eq. 2}$$

where i_{peak} is the peak current (oxidation in this case), n is the number of transferred electrons (here $n = 1$), F is the Faraday's constant, D is the diffusion coefficient of the redox probe (here $D = 7.63e^{-6}$ $cm^2 s^{-1}$), R is the universal gas constant, T is the temperature, C is the concentration of the redox probe, A is the ECSA, and ΔE_{peak} is the oxidation-reduction peak separation in mV.

ECSA is increased by 1.3 times with bare LIG compared to the geometric area (0.9 mm^2), while the enhancement is 4 times in $eMoS_x$-LIG. Comparing k^0 of LIG to $eMoS_x$-LIG shows an improvement of 50%. These results confirm that electrodeposition of MoS_x significantly improves the electrochemical properties of LIG. Previous studies have also reported improved electrochemical properties by the addition of transition-metal dichalcogenides (TMDs) [51]. Hence, $eMoS_x$-LIG electrodes are used for TYR and UA quantification in the following sections, unless otherwise stated. We also tested the shelf-life of $eMoS_x$-LIG sensors (Fig. S5, SI, Section S8). It is found that the sensors stored in the N_2 inert environment are stable for two weeks and then started degrading, however the sensors stored in ambient air started degrading after one week.

3.2. Off-chip, multimodal measurements

The $eMoS_x$-LIG sensor is first tested with TYR and UA in artificial saliva with DPV, SWV, and LAACV. Fig. 2a shows the DPV response of a representative sensor to TYR and UA in artificial saliva for concentrations ranging from 150 nM to 1 mM. TYR and UA have distinct and separate oxidation peaks evident from the results. Fig. 2b shows estimated LOD values for TYR and UA using SWV and DPV data (separately). The peak heights are extracted from the raw data manually after baseline subtraction and the linear range of the sensor is identified. The LOD is defined as the concentration at the intersection of the linear fit of the response to the baseline variation magnitude. In this analysis, since the baseline is subtracted prior to LOD estimation, $3.3\sigma_{baseline}$ is used to estimate LOD (the gray-shaded regions in Fig. 2b). The calculated LOD values for TYR and UA in artificial saliva are found to be 116 uM and 3.5 uM with SWV, and 21 uM and 1.2 uM with DPV.

Interestingly, while SWV shows similar sensitivity to DPV for TYR (in linear scale: SWV 4.1 mAM^{-1}; DPV 4.5 mAM^{-1}), it has slightly higher sensitivity for UA (in linear scale: SWV 27.8 mAM^{-1}; DPV 19.6 mAM^{-1}). In contrast, DPV offers a much lower LOD and wider linear range for both analytes. The enhanced background rejection of pulse-based techniques such as DPV and SWV is due to the difference in decay rates of the faradaic and non-faradaic currents. Such background rejection makes them more sensitive as compared to linear sweep voltammetry methods [52]. In particular, it has been previously reported that SWV is superior compared to other methods when reversible and quasi reversible reactions are concerned, however limited with sluggish reactions (i.e. when there is a large potential difference between anodic and cathodic peaks [53]), as is the case in the present work for UA and TYR (see CV curves in Fig. S8). As such, we believe that because of the poor reaction reversibility, the DPV method performs better (lower LOD and wider linear range) compared to SWV, which is consistent with prior works [54]. Previous studies have also shown the difference in performance when comparing SWV and DPV [52,54,55].

Conventional electrochemical analytical methods usually house a circuit that can apply potential waveforms and read the current which is then used as the signal to detect the target molecules. While simple amperometry at a constant applied potential is extensively used, more complex input waveforms, such as ramps (CV), saw-tooth (Linear sweep voltammetry; LSV), and pulse voltammetry (SWV, DPV) produce commensurate outputs which could be used to extract more information about the system. The processed output data generally consists of peaks that correspond to different oxidation and reduction potentials of the

Table 1
The calculated electrochemically active surface area (ECSA) and the heterogenous electron transfer rate constant (k^0) and comparison between LIG and $eMoS_x$-LIG.

	ECSA (mm^2)	k^0 (x 10^{-3} cm/s)
LIG	1.20	1.43
$eMoS_x$-LIG	3.69	2.18

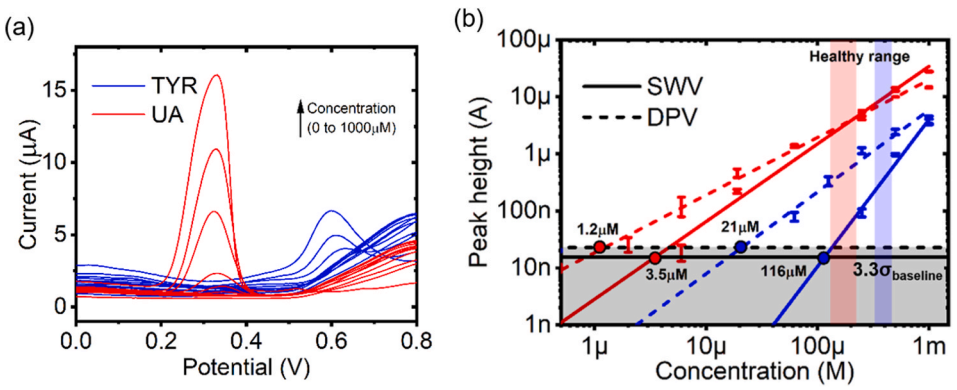

Fig. 2. Sensor performance defined using traditional strategy in electrochemical sensors. (a) Representative differential pulse voltammetry (DPV) curves with eMoS$_x$-LIG sensor in response to uric acid (UA; red) and tyrosine (TYR; blue) in artificial saliva. (b) Calibration curves obtained using DPV (dashed) and square wave voltammetry (SWV; solid) after baseline subtraction. Limit of detection (LOD) is extracted and values are added on the plots for each method. The gray shaded area shows the blank current variation ($3.3\sigma_{baseline}$, where $\sigma_{baseline}$ is the standard deviation of baseline). Healthy concentration range for TYR and UA in saliva are depicted by vertical shaded bands. (Error bars: standard deviation, Number of data points in each error bar: 3, total number of devices: 2). (For interpretation of the references to colour in this figure legend, the reader is referred to the Web version of this article.)

involved species. Some species might undergo several intermediate oxidation-reduction steps and produce several peaks, especially if the measurement is repeated several times with the same sample solution [56]. Usually, for quantitative analysis of a specific analyte, the most prominent peak among these is selected and its magnitude is used to estimate the concentration of the analyte (as also demonstrated in Fig. 2b).

It has been shown that data fusion could enhance the sensitivity of electrical sensors, such as physiological sensors for measuring body movements and applied forces, pressure sensors, and skin/chest/scalp electrodes for monitoring electrocardiogram (ECG), electromyogram (EMG), and electroencephalogram (EEG) signals [57]. Hence, measuring/fusing multiple electrochemical peaks/signatures could also be beneficial for electrochemical sensors. However, processing the data is challenging, especially when multiple analytes are involved. More advanced electrochemical methods, such as semicircular voltammetry (SCV) [58] or large amplitude AC voltammetry (LAACV) methods [23] apply complicated waveforms to the working electrode measuring a complex current which is rather hard to infer from without further processing. The idea of probing the system with a complex input has been theorized to provide a lot of data which could be used to increase the sensitivity and selectivity of the sensor [22]. In the following sections, we explore this idea and demonstrate that multiplexed detection can be achieved with high accuracy by using multimodal sensing and machine learning (ML), achieving LODs more than 2 orders of magnitude lower than the single-peak, single-voltammetry methods shown in Fig. 2. It should be noted that using single DPV peak analysis, Yang et al. [60] demonstrated a wearable sensor solely based on LIG for detecting UA and TYR down to 0.74 μM and 3.6 μM in sweat in pH 4.6. In comparison, our ML-based multimodal analytical device in this paper enables selective and sensitive detection of UA and TYR with LOD of 10 *nM* and 100 *nM*, respectively, in saliva and sweat in pH 6.7 (neutral solution).

To develop, train, test, and implement ML models, we built a customized setup capable of multimodal measurements through automated data collection and processing (details about the hardware and software setups are provided in Section 2.2 and in Fig. S1, SI, Section S3 and Fig. S2, SI, Section S4). An example LAACV result is shown in Fig. S7 (SI, Section S10), showing the various harmonics that could be extracted from the LAACV data. The DC component corresponds to the cyclic voltammetry (CV) data (example CV curves shown in Figs. S8c–d, SI, Section S11), whereas the higher harmonics have varied peaks which help extract more features for training the ML model. Other methods used in this paper, such as SWV (example SWV curves shown in Figs. S8a–b, SI, Section S11) and DPV, focus only on the oxidation reaction of the analytes missing out on the reduction cycle, however LAACV contains data for both forward and reverse scans, i.e. the oxidation and reduction cycles, providing more information about the reactions occurring with the analytes, and hence adding to the feature space for ML training.

3.3. Development and optimization of the machine learning model

The raw data obtained from the sensors varies with respect to the peak currents, baseline fluctuation, and sensor-sensor variation. In order to train the ML model, the features should be extracted from the raw data. The raw data is first checked using a script to get rid of any obvious outliers using specific hardcoded conditions (bad electrical connection, instrumentation failure, failed passivation resulting in erratic signal, etc.). Then the raw data for each electrochemical module – DPV, SWV, and LAACV – is processed as follows:

For each module, a specific preset constraint is set with respect to the constituent gaussian peak heights, locations, and widths. Then these peaks are fit to best represent the raw DPV (Fig. S9a, SI, Section S12), SWV (Fig. S9b, SI, Section S12), and LAACV (Fig. S7, SI, Section S10) data. An optimization algorithm is developed to decompose each individual measurement into its constituent parabolic baseline and gaussian peaks by fitting their sum to the raw data as shown in Fig. S7. Initial constraints are chosen to fit most of the data. Once all the raw data of a module are fit, a second run is performed similarly with tighter constraints. The tighter constraints are obtained from the first fit. The upper limit is chosen as the 99th percentile value of the first fit and the lower value is chosen as the 1st percentile. This eliminates outliers and allows the model to have tight enough constraints to prevent overfitting [61]. The resulting fit parameters from the second run (gaussian peak heights, locations, widths) are used as features to train and test the ML algorithms. This process is schematically described in Fig. 3.

Several architectures and core ML algorithms including linear regression (LR), support vector regressor (SVR), k-Nearest neighbors (kNN), decision tree regressor (DT), and Bayesian ridge (BR) are tested with the data to identify the optimized model. Mainly, we focus on supervised machine learning models that could be used for regression. For all models, leave-one-out cross validation [62] is utilized to maximize the data usage for testing. A thousand runs of these tests are performed in which 90% of the data is used for training and the remaining 10% of the unseen data is used for testing. In order to accommodate two analytes under test, either multiclass regression algorithms are used, or multiple single class regression algorithms are collated by the architecture to emulate a multiclass regressor. A two-step accept-reject classifier is also used to determine if the given measurement is within the threshold of detection of the system to prevent false positives and negatives by the main classifier.

All the features extracted from each of the electrochemical modules are collated and used to train and test the ML models. To obtain an

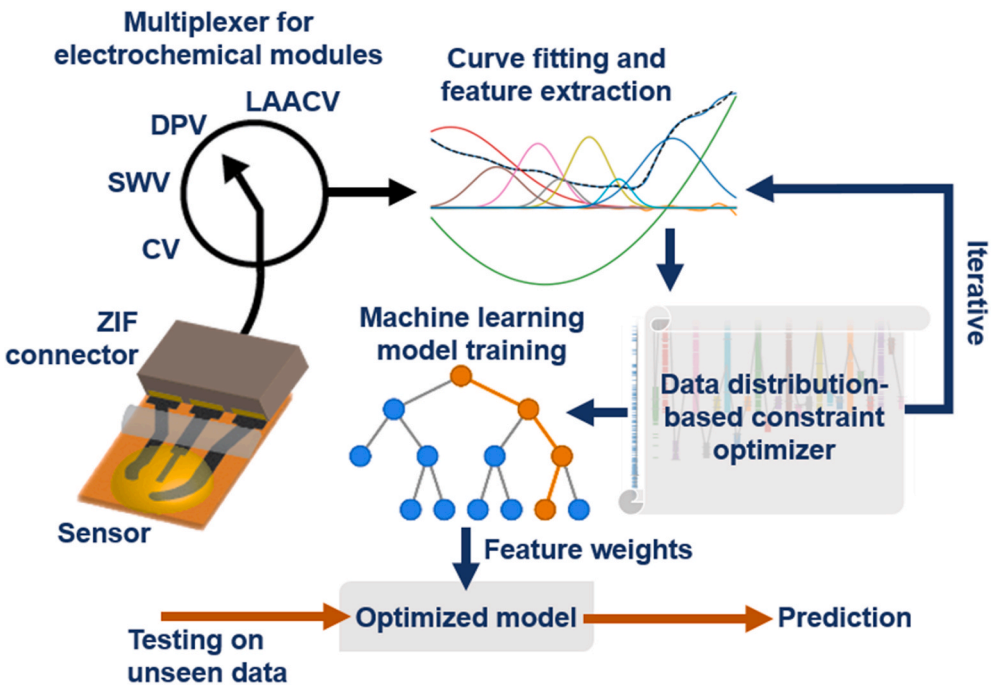

Fig. 3. Data collection, pre-processing, and machine learning analysis. Schematic flow chart depicting the electrochemical measurement modules, data flow, and data processing steps for training and testing the machine learning model. First, the multiplexer automatically chooses the electrochemical module to test using a developed script. Electrochemical modules include cyclic voltammetry (CV), square wave voltammetry (SWV), differential pulse voltammetry (DPV), and large amplitude AC voltammetry (LAACV). The raw data is processed to extract the constituent peaks and used to train the machine learning model through an iterative process using a data distribution based fit-constraint optimizer. The optimized model is used to test on unseen data to predict the analyte and its concentration.

optimum architecture, two designs are investigated (named as one-step regressor and two-step regressor). Before discussing each method, we should highlight that in order to quantify the sensitivity of each architecture, a threshold concentration (TC) is defined to easily compare between models. TC is defined as the concentration c at which $R^2|1-m|^{-1}$ is maximized if a linear fit is made between concentration c and the highest concentration, where m is the slope and R^2 is the R-squared parameter corresponding to the fit. This would in essence maximize the fit such that the slope is nearly ideal. By comparing the TC values, the chosen features, ML algorithm, and architecture are optimized.

One-step regressor: First, a single multi-class regressor is used to predict the concentrations of both TYR and UA. In this case, among

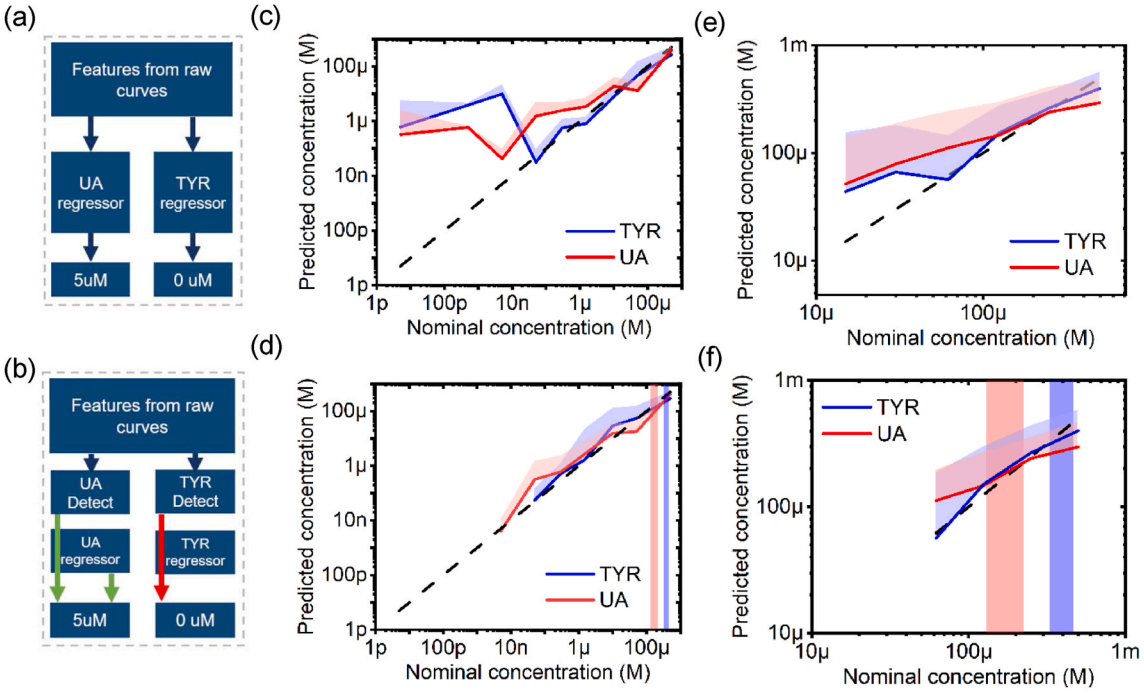

Fig. 4. Effect of model architecture on performance of the ML-powered electrochemical biosensor. Machine learning with a (a) one-step and (b) two-step regressor architecture. Predicated vs. nominal concentration of UA and TYR obtained using (c) the one-step regressor and (d) the two-step classifier with single analyte spiked in artificial saliva. (e) and (f) plot the results with one-step and two-step architectures, respectively, in mixture of TYR and UA. In parts d and f, the vertical bands represent physiological concentration of UA (red) and TYR (blue) in saliva of healthy people. (Error bars: standard deviation, Number of data points in each error bar: > 300, total number of devices: 16). (For interpretation of the references to colour in this figure legend, the reader is referred to the Web version of this article.)

several algorithms, kNN algorithm and DT provide the best accuracy (Table S3, SI, Section S13). Next, we investigate a two single-class regressors to de-couple the analytes. This method yields a higher accuracy for each analyte, as each regressor is focused on one analyte. Fig. 4a plots the schematic of this architecture and Fig. 4c shows the output of the DT regressor plotted against the expected output (concentration). One can observe that at higher concentrations, the expectation is met, however at lower concentrations, the model underperforms, and the output is noisy. With each analyte having its own classification algorithm, it is found that the decision tree (DT) algorithm is the best considering the accuracies obtained (Table S4, SI, Section S13).

As several electrochemical modules are utilized for data collection, combinations of these methods are utilized to identify the best methods to use for each analyte. While comparing algorithms, the best among all the permutations and combinations is considered. SWV and DPV are considered as individual methods and LAACV is considered as four methods with the DC component being one, and the three harmonics being the other three methods. Hence, total of six methods are screened, and the best combination is identified (Table S5, SI, Section S13). As can be seen, combination of SWV, DPV, and LAACV (last row in Table S5, SI, Section S13) provides the lowest overall TC among all other combinations, highlighting the power of data fusion.

Two-step regressor: In order to set the LOD to TC, a second binary classifier is trained to identify whether the given data contains target concentrations above the TC, hence setting LOD as TC. The binary classifier screens the features to identify whether that particular analyte is present in measurable quantity, and if not, the second classifier would be overruled and a zero would be the output as shown schematically in Fig. 4b. The addition of a binary classifier results in the output plotted in Fig. 4d and is used to quantify the LOD of the sensor. It is found that TYR and UA with LODs of 100 *nM* and 10 *nM*, respectively, can be detected which is at least an improvement of two orders of magnitude from the method shown in Fig. 2b. This enhancement in LOD is attributed to the inclusion of data of the full potential scan window rather than just a single peak across different electrochemical modules and data fusion across SWV, DPV, and LAACV which the ML model uses to learn subtle patterns. This enhancement in the prediction capabilities demonstrates the effectiveness of the proposed ML-based analytical method for sensors.

3.4. Multiplexed detection in mixtures using machine learning

The model trained from the independent target analyte concentrations is used along with the training data from the mixed analyte data to predict the mixed analyte concentration. The architecture shown in Fig. 4b is utilized in order to obtain the LOD of the sensors and as seen from Fig. 4f, the linear region is well within the physiological limits. It is observed that when the training data only consists of single analyte data without any intermixing and the model is tested on data from mixed samples, the model performs poorly with the outputs having no linear region, hence a TC of ~500 μM. However, when both mixed and single analyte data are used for training and unseen mixed data is tested, the model performance improves substantially with improved LODs of 60 μM and 60 μM for TYR and UA, respectively as shown in Fig. 4f (improvement from Fig. 4e by the two-step regressor architecture for LOD definition). This disparity between the performance may be because the model learns better to isolate and independently learn characteristics of each analyte eliminating common peaks that may arise between different analytes when it is trained on both mixed and single analyte data, which is not possible when it is just trained on the single analyte data.

3.5. On-chip sweat analysis with a flexible sensing patch

Similar to saliva tests, the developed ML-based approach also shows a linear response in sweat within the physiological window (Fig. 5a). The physiological concentration of TYR and UA in sweat is 40 μM and 170 μM. Multimodal data is collected using an on-chip device (with pseudo-reference electrode) and the best performing ML algorithm (i.e., two step regressor with DT algorithm) is implemented.

In addition to off-body tests, in order to demonstrate the application of eMoS$_x$-LIG sensor for wearable applications, on-body characterization of the sensor is performed for detecting TYR and UA in artificial sweat. To evaluate the flexibility of the sensor, eMoS$_x$-LIG based sensors with on chip pseudo reference electrode were fabricated and tested in a home-built custom bending setup shown in Fig. S6a. TYR and UA of 500 *uM* concentration in artificial sweat were added to the sensor and various radii of curvature *R* were used for bending the sensor both in positive (lateral stretch of LIG film) and negative (lateral compression of LIG film) directions. The lowest magnitude of *R* achieved was 3.5 *mm*. It was found that even at this high bending force, the sensor response in the form of DPV peak height only changed by a maximum of 15% as compared to when the sensor was flat shown in Fig. 5b (DPV curves are shown in Fig. S6b).

Finally, application of the on-chip device for on-body sweat analysis is demonstrated (Fig. 5c). The sensor is prepared as described previously using MoS$_x$ electrodeposition on LIG working electrode. However, instead of using silicone to passivate the sensor, the sensor is first stuck onto a commercial medical polyurethane (MPU) sheet (Tegaderm, 3M) upon which transparent nail polish is applied to passivate the sensor. Nail polish is chosen for passivation to reduce the thickness of the final sensor. Insulated single-strand copper wire is used to make electrical contacts to LIG contact pads using carbon paste which is air dried after application. A second layer of nail polish is applied over the electrical

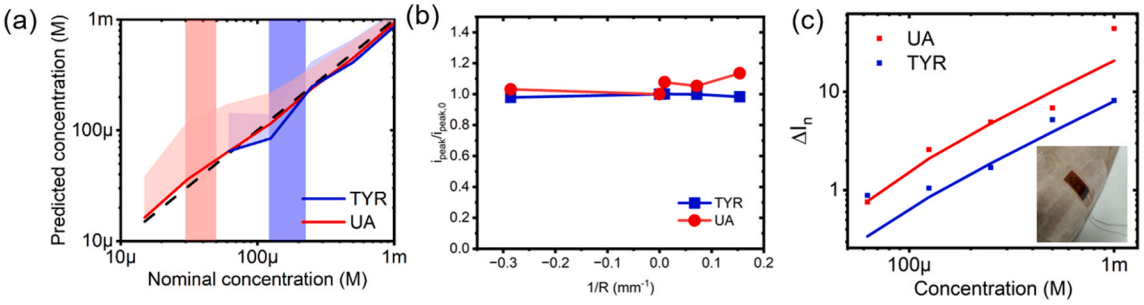

Fig. 5. Sweat analysis with on-chip device, flexibility analysis, and on-body testing. (a) Machine learning-based response to analytes in artificial sweat using eMoS$_x$-LIG sensor with on-chip electrodes showing linearity within the physiologically relevant range (shaded vertical regions). The best performing algorithm is implemented. (Error bars: standard deviation, Number of data points in each error bar: >300, total number of devices: 8). (b) The peak current of DPV data with TYR and UA of 500 *uM* concentration changes by a maximum of 15% under extreme bending (R = radius of bending curvature at the sensor). Both bending to compress the LIG film laterally (negative *R*) and stretch the LIG film laterally (positive *R*) were carried out. (c) On-body sensor response using DPV measurement of TYR and UA in artificial sweat with on-chip electrodes. The figure plots change in peak amplitude ΔI_n vs. the analyte concentration. Inset shows the body-worn sensor.

contacts to prevent any unintended electrochemical reactions. The sensor package is then attached on the arm and artificial sweat with various concentrations of TYR and UA are injected between the sensor and skin using a blunt syringe. DPV readout (as example) is carried out by closing the MPU patch. Fig. 5c shows the measurement results indicating successful detection of TYR and UA plotting $\Delta I_n = \frac{I-I_0}{I_0}$ where I is the DPV peak amplitude and I_0 is the baseline. The signal change is plotted against the concentration and a linearity with R^2-value of 95% for TYR and 85% for UA is found, confirming good linearity of the wearable sensor.

4. Conclusions

In this work, we developed a novel analytical method based on convergence of machine learning with multimodal electrochemical sensing and demonstrated its application with printed eMoS$_x$-LIG flexible sensors to achieve simultaneous quantification of UA and TYR with LOD well below the physiological concentration in saliva and sweat. We developed an algorithm for automatic baseline subtraction with integrated feature extraction to process SWV, DPV, and LAACV data and to produce features to train a machine learning model. Single-peak analysis to measure the analyte concentration is compared to the developed optimized machine learning model. It is shown that owing to the multimodal and multipeak analysis, the method is able to reduce LOD by two orders of magnitude. In this study, apart from the improvement of LODs, three main insights can be obtained as follows: (a) Firstly, material engineering in the form of electrodeposition of MoS$_x$ is performed, resulting in the improvement of the electrochemical (from CV measurements) and physical surface area (from BET measurements), as well as the heterogenous electron transfer rates (discussed in Section 3.1). (b) Secondly, because of the variation in response of different electrochemical methods, multimodal effects are studied and reported which calls for further studies regarding comparison of multiple electrochemical methods in bioanalytical systems; and (c) thirdly, due to the variable response of various electrochemical modules, data processing and fusion techniques lead to analytical improvement which we attribute to inclusion of multiple peaks in the analysis as compared to conventional single-peak analysis, further highlighting the benefits of multimodal electrochemical data fusion. We showed that the model is able to selectively quantify each analyte in a mixture and hence, achieving multiplexed detection using a single sensor. On-body measurements using a wearable patch also show favorable results for detection of TYR and UA in sweat. The machine learning-powered electrochemical diagnostic approach presented in this paper may find broader application in multiplexed biochemical sensing. For example, this method can be extended to a variety of other analytes – including catecholamine neurotransmitters – which are traditionally challenging to detect using electrochemical sensors due to similarity in molecular structure and overlapping redox potentials [63]. Combined with innovations in material and device engineering for sensor development, analytical methods such as this work may provide unprecedented opportunities in pharmaceuticals, life science research, food screening, detection of environmental toxins, and biodefense, where accurate and multiplexed POC testing or in-line monitoring is needed.

CRediT authorship contribution statement

Vinay Kammarchedu: Conceptualization, Methodology, Software, Validation, Formal analysis, Investigation, Data curation, Writing – original draft, Writing – review & editing, Visualization. **Derrick Butler:** Investigation, Methodology, Writing – review & editing. **Aida Ebrahimi:** Conceptualization, Methodology, Writing – review & editing, Supervision, Funding acquisition.

Declaration of competing interest

The authors declare that they have no known competing financial interests or personal relationships that could have appeared to influence the work reported in this paper.

Data availability

Data will be made available on request.

Acknowledgment

The authors would like to thank the support from NSF:I/UCRC Phase II: Center for Atomically Thin Multifunctional Coatings (ATOMIC; Award #2113864). V. K. also thanks the Center for Biodevices (CfB) at Pennsylvania State University for the Leighton Riess Graduate Fellowship in Engineering. The authors thank Dr. Nichole M. Wonderling and Bob Scandle at the Materials Characterization Lab (MCL, Penn State University) for their help with XRD and BET measurement and analysis.

Appendix A. Supplementary data

Supplementary data to this article can be found online at https://doi.org/10.1016/j.aca.2022.340447.

References

[1] A. Romeo, T.S. Leung, S. Sánchez, Smart biosensors for multiplexed and fully integrated point-of-care diagnostics, Lab Chip 16 (11) (May 2016) 1957–1961, https://doi.org/10.1039/C6LC90046A.
[2] P.S. Pakchin, S.A. Nakhjavani, R. Saber, H. Ghanbari, Y. Omidi, Recent advances in simultaneous electrochemical multi-analyte sensing platforms, TrAC, Trends Anal. Chem. 92 (Jul. 2017) 32–41, https://doi.org/10.1016/J.TRAC.2017.04.010.
[3] A. Jones, L. Dhanapala, R.N.T. Kankanamage, C.V. Kumar, J.F. Rusling, Multiplexed immunosensors and immunoarrays, Anal. Chem. 92 (1) (Jan. 2020) 345–362, https://doi.org/10.1021/acs.analchem.9b05080.
[4] P. Song, N.D. Hershey, O.S. Mabrouk, T.R. Slaney, R.T. Kennedy, Mass spectrometry 'sensor' for in vivo acetylcholine monitoring, Anal. Chem. 84 (11) (Jun. 2012) 4659–4664, https://doi.org/10.1021/AC301203M.
[5] D. Morin, B. Grasland, K. Vallée-Réhel, C. Dufau, D. Haras, On-line high-performance liquid chromatography-mass spectrometric detection and quantification of N-acylhomoserine lactones, quorum sensing signal molecules, in the presence of biological matrices, J. Chromatogr. A 1002 (1–2) (Jun. 2003) 79–92, https://doi.org/10.1016/S0021-9673(03)00730-1.
[6] J. Perumal, Y. Wang, A. Binte, E. Attia, U.S. Dinish, M. Olivo, Towards a point-of-care SERS sensor for biomedical and agri-food analysis applications: a review of recent advancements, Nanoscale 13 (2021) 553, https://doi.org/10.1039/d0nr06832b.
[7] W. Zhang, W. Ruiguo, P. Wang, R. Wang, Z. Lin, Miniaturized electrochemical sensors and their point-of-care applications, Electrochem. commun. (2019), https://doi.org/10.1016/j.cclet.2019.09.022.
[8] P. Bollella, et al., Beyond graphene: electrochemical sensors and biosensors for biomarkers detection, Biosens. Bioelectron. 89 (Mar. 2017) 152–166, https://doi.org/10.1016/J.BIOS.2016.03.068.
[9] J.A. Ribeiro, P.M.V. Fernandes, C.M. Pereira, F. Silva, Electrochemical sensors and biosensors for determination of catecholamine neurotransmitters: a review, Talanta 160 (Nov. 2016) 653–679, https://doi.org/10.1016/J.TALANTA.2016.06.066.
[10] Y. Lei, et al., Single-atom doping of MoS2with manganese enables ultrasensitive detection of dopamine: experimental and computational approach, Sci. Adv. 6 (32) (Aug. 2020) 4250–4257, https://doi.org/10.1126/sciadv.abc4250.
[11] D. Butler, D. Moore, N.R. Glavin, J.A. Robinson, A. Ebrahimi, Facile post-deposition annealing of graphene ink enables ultrasensitive electrochemical detection of dopamine, ACS Appl. Mater. Interfaces 13 (9) (Mar. 2021) 11185–11194, https://doi.org/10.1021/acsami.0c21302.
[12] R. Muralidharan, V. Chandrashekhar, D. Butler, A. Ebrahimi, A smartphone-interfaced, flexible electrochemical biosensor based on graphene ink for selective detection of dopamine, IEEE Sensor. J. 20 (22) (Nov. 2020) 13204–13211, https://doi.org/10.1109/JSEN.2020.3005171.
[13] S. Duanghathaipornsuk, et al., Detection technologies for reactive oxygen species: fluorescence and electrochemical methods and their applications, Vol. 11, Page 30, Biosensors 11 (2) (2021) 30, https://doi.org/10.3390/BIOS11020030. Jan. 2021.
[14] A. Ebrahimi, et al., FeSx-graphene heterostructures: nanofabrication-compatible catalysts for ultra-sensitive electrochemical detection of hydrogen peroxide, Sensor. Actuator. B Chem. 285 (Apr. 2019) 631–638, https://doi.org/10.1016/J.SNB.2018.12.033.

[15] S. Borgmann, Electrochemical quantification of reactive oxygen and nitrogen: challenges and opportunities, Anal. Bioanal. Chem. 394 (1) (May 2009) 95–105, https://doi.org/10.1007/s00216-009-2692-1.
[16] T. Wu, A. Alharbi, R. Kiani, D. Shahrjerdi, Quantitative principles for precise engineering of sensitivity in graphene electrochemical sensors, Adv. Mater. 31 (6) (2019) 1–12, https://doi.org/10.1002/adma.201805752.
[17] Y. Uchida, E. Kätelhön, R.G. Compton, Sweep voltammetry with a semi-circular potential waveform: electrode kinetics, J. Electroanal. Chem. 835 (Feb. 2019) 60–66, https://doi.org/10.1016/j.jelechem.2018.12.030.
[18] Y. Oh, et al., Tracking tonic dopamine levels in vivo using multiple cyclic square wave voltammetry, Biosens. Bioelectron. 121 (Dec. 2018) 174–182, https://doi.org/10.1016/J.BIOS.2018.08.034.
[19] C. Park, et al., Fast cyclic square-wave voltammetry to enhance neurotransmitter selectivity and sensitivity, Anal. Chem. 90 (22) (Nov. 2018) 13348–13355, https://doi.org/10.1021/acs.analchem.8b02920.
[20] B. Habibi, M.H. Pournaghi-Azar, Simultaneous determination of ascorbic acid, dopamine and uric acid by use of a MWCNT modified carbon-ceramic electrode and differential pulse voltammetry, Electrochim. Acta 55 (19) (Jul. 2010) 5492–5498, https://doi.org/10.1016/J.ELECTACTA.2010.04.052.
[21] A.A. Ensafi, M. Taei, T. Khayamian, A. Arabzadeh, Highly selective determination of ascorbic acid, dopamine, and uric acid by differential pulse voltammetry using poly(sulfonazo III) modified glassy carbon electrode, Sensor. Actuator. B Chem. 147 (1) (May 2010) 213–221, https://doi.org/10.1016/J.SNB.2010.02.048.
[22] L. Gundry, et al., Recent advances and future perspectives for automated parameterisation, Bayesian inference and machine learning in voltammetry, Chem. Commun. 57 (15) (Feb. 2021) 1855–1870, https://doi.org/10.1039/d0cc07549c.
[23] H. Adamson, A.M. Bond, A. Parkin, Probing biological redox chemistry with large amplitude Fourier transformed ac voltammetry, Chem. Commun. 53 (69) (Aug. 2017) 9519–9533, https://doi.org/10.1039/C7CC03870D.
[24] F. Cui, Y. Yue, Y. Zhang, Z. Zhang, H.S. Zhou, Advancing biosensors with machine learning, ACS Sens. 5 (2020) 3364, https://doi.org/10.1021/acssensors.0c01424.
[25] L.B. Ayres, F.J.V. Gomez, J.R. Linton, M.F. Silva, C.D. Garcia, Taking the leap between analytical chemistry and artificial intelligence: a tutorial review, Anal. Chim. Acta 1161 (May 2021), https://doi.org/10.1016/J.ACA.2021.338403.
[26] J. Massah, K. Asefpour Vakilian, An intelligent portable biosensor for fast and accurate nitrate determination using cyclic voltammetry, Biosyst. Eng. 177 (Jan. 2019) 49–58, https://doi.org/10.1016/J.BIOSYSTEMSENG.2018.09.007.
[27] K.T. Kishida, et al., Subsecond dopamine fluctuations in human striatum encode superposed error signals about actual and counterfactual reward, Proc. Natl. Acad. Sci. U.S.A. 113 (1) (Jan. 2016) 200–205, https://doi.org/10.1073/pnas.1513619112.
[28] R.J. Moran, et al., The protective action encoding of serotonin transients in the human brain, Neuropsychopharmacology 43 (6) (2018) 1425–1435, https://doi.org/10.1038/npp.2017.304, 436, Jan. 2018.
[29] N. Liu, W. Ye, G. Liu, G. Zhao, Improving the accuracy of stripping voltammetry detection of Cd2+ and Pb2+ in the presence of Cu2+ and Zn2+ by machine learning: understanding and inhibiting the interactive interference among multiple heavy metals, Anal. Chim. Acta 1213 (Jun. 2022), 339956, https://doi.org/10.1016/J.ACA.2022.339956.
[31] Y. Sheng, et al., Electrochemical detection combined with machine learning for intelligent sensing of maleic hydrazide by using carboxylated PEDOT modified with copper nanoparticles, Microchim. Acta 186 (8) (2019), https://doi.org/10.1007/s00604-019-3652-x.
[32] S.C. Daubner, T. Le, S. Wang, Tyrosine hydroxylase and regulation of dopamine synthesis, Arch. Biochem. Biophys. 508 (1) (Apr. 2011) 1–12, https://doi.org/10.1016/J.ABB.2010.12.017.
[33] S.N. Young, L-tyrosine to alleviate the effects of stress? J. Psychiatry Neurosci. 32 (3) (May 2007) 224.
[34] A. Srivastava, A.D. Kaze, C.J. McMullan, T. Isakova, S.S. Waikar, Uric acid and the risks of kidney failure and death in individuals with CKD, Am. J. Kidney Dis. 71 (3) (Mar. 2018) 362, https://doi.org/10.1053/J.AJKD.2017.08.017.
[35] H.K. Choi, D.B. Mount, A.M. Reginato, Pathogenesis of gout, Ann. Intern. Med. 143 (7) (2005) 499–516, https://doi.org/10.7326/0003-4819-143-7-200510040-00009.
[36] D.I. Feig, D.-H. Kang, R.J. Johnson, Uric acid and cardiovascular risk, N Engl J Med. 359 (17) (Jun. 2009) 1811–1821, https://doi.org/10.1056/NEJMra0800885, doi: 10.1056/NEJMRA0800885.
[37] R. Ye, D.K. James, J.M. Tour, Laser-Induced Graphene (2018), https://doi.org/10.1021/acs.accounts.8b00084.
[38] A. Behrent, C. Griesche, P. Sippel, A.J. Baeumner, Process-property correlations in laser-induced graphene electrodes for electrochemical sensing, Microchim. Acta 188 (5) (May 2021) 1–14, https://doi.org/10.1007/s00604-021-04792-3.
[39] K. Zhou, et al., Electrochemical Sensors Based on MoSx-Functionalized Laser-Induced Graphene for Real-Time Monitoring of Phenazines Produced by Pseudomonas aeruginosa, Advanced Healthcare Materials (2022), https://doi.org/10.1002/adhm.202200773.
[40] F. Pedregosa Fabianpedregosa, et al., Scikit-learn: machine learning in Python, J. Mach. Learn. Res. 12 (85) (2011) 2825–2830.
[41] C.R. Harris, et al., Array programming with NumPy, Nat 585 (7825) (Sep. 2020) 357–362, https://doi.org/10.1038/s41586-020-2649-2, 2020 5857825.
[42] P. Virtanen, et al., SciPy 1.0: fundamental algorithms for scientific computing in Python, Nat. Methods 17 (3) (Mar. 2020) 261–272, https://doi.org/10.1038/S41592-019-0686-2.
[43] M. Mathew, S. Radhakrishnan, A. Vaidyanathan, B. Chakraborty, C.S. Rout, Flexible and wearable electrochemical biosensors based on two-dimensional materials: recent developments, Anal. Bioanal. Chem. 413 (3) (Oct. 2020) 727–762, https://doi.org/10.1007/S00216-020-03002-Y, 2020 4133.
[44] E.A. Ponomarev, M. Neumann-Spallart, G. Hodes, C. Lévy-Clément, Electrochemical deposition of MoS2 thin films by reduction of tetrathiomolybdate, Thin Solid Films 280 (1–2) (1996) 86–89, https://doi.org/10.1016/0040-6090(95)08204-2.
[45] L. Mai, et al., Molybdenum oxide nanowires: synthesis & properties, Mater. Today 14 (7–8) (Jul. 2011) 346–353, https://doi.org/10.1016/S1369-7021(11)70165-1.
[46] J. Lin, et al., Laser-induced porous graphene films from commercial polymers, Nat. Commun. 5 (1) (Dec. 2014) 5714, https://doi.org/10.1038/ncomms6714.
[47] V.V.T. Doan-Nguyen, et al., Molybdenum polysulfide chalcogels as high-capacity, anion-redox-driven electrode materials for Li-ion batteries, Chem. Mater. 28 (22) (2016) 8357–8365, https://doi.org/10.1021/acs.chemmater.6b03656.
[48] L.X. Duy, Z. Peng, Y. Li, J. Zhang, Y. Ji, J.M. Tour, Laser-induced graphene fibers, Carbon N. Y. 126 (Jan. 2018) 472–479, https://doi.org/10.1016/J.CARBON.2017.10.036.
[49] Y.M. Wang, D.D. Zhao, Y.Q. Zhao, C.L. Xu, H.L. Li, Effect of electrodeposition temperature on the electrochemical performance of a Ni(OH)2 electrode, RSC Adv. 2 (3) (Jan. 2012) 1074–1082, https://doi.org/10.1039/C1RA00613D.
[50] J. Lin, et al., Laser-induced porous graphene films from commercial polymers, Nat. Commun. 5 (2014) 5714, https://doi.org/10.1038/NCOMMS6714.
[51] A. Chhetry, M. Sharifuzzaman, H. Yoon, S. Sharma, X. Xuan, J. Yeong Park, MoS 2-decorated laser-induced graphene for a highly sensitive, hysteresis-free, and reliable piezoresistive strain sensor, ACS Appl. Mater. Interfaces (2019), https://doi.org/10.1021/acsami.9b04915.
[52] A. Chen, B. Shah, Electrochemical sensing and biosensing based on square wave voltammetry, Anal. Methods, doi:10.1039/c3ay40155c.
[53] D. Guziejewski, L. Stojanov, R. Gulaboski, V. Mirceski, Reversible and quasireversible electron transfer under conditions of differential square-wave voltammetry, J. Phys. Chem. C 126 (12) (Mar. 2022) 5584–5591, https://doi.org/10.1021/acs.jpcc.2c01188.
[54] L.C.S. Figueiredo-Filho, T.A. Silva, F.C. Vicentini, O. Fatibello-Filho, Simultaneous voltammetric determination of dopamine and epinephrine in human body fluid samples using a glassy carbon electrode modified with nickel oxide nanoparticles and carbon nanotubes within a dihexadecylphosphate film †, Analyst (2014) https://doi.org/10.1039/c4an00229f.
[55] G. Hussain, D.S. Silvester, Comparison of voltammetric techniques for ammonia sensing in ionic liquids, Electroanalysis 30 (1) (Jan. 2018) 75–83, https://doi.org/10.1002/ELAN.201700555.
[56] Y. Zeng, J. Yang, K. Wu, Electrochemistry and determination of epinephrine using a mesoporous Al-incorporated SiO2 modified electrode, Electrochim. Acta 53 (14) (May 2008) 4615–4620, https://doi.org/10.1016/J.ELECTACTA.2008.01.011.
[57] R. Gravina, P. Alinia, H. Ghasemzadeh, G. Fortino, Multi-sensor fusion in body sensor networks: State-of-the-art and research challenges, Inf. Fusion 35 (May 2017) 68–80, https://doi.org/10.1016/J.INFFUS.2016.09.005.
[58] Y. Wang, R.G. Compton, Semi-circular sweep voltammetry. Bio-analytical applications, Biosens. Bioelectron. 179 (May 2021), 113083, https://doi.org/10.1016/J.BIOS.2021.113083.
[60] Y. Yang, et al., A laser-engraved wearable sensor for sensitive detection of uric acid and tyrosine in sweat, Nat. Biotechnol. 38 (2) (Feb. 2020) 217–224, https://doi.org/10.1038/S41587-019-0321-X.
[61] X. Ying, An overview of overfitting and its solutions. J. Phys: Conference series. Vol. 1168. No. 2. IOP Publishing, 2019.
[62] T.T. Wong, Performance evaluation of classification algorithms by k-fold and leave-one-out cross validation, Pattern Recogn. 48 (9) (Sep. 2015) 2839–2846, https://doi.org/10.1016/J.PATCOG.2015.03.009.
[63] B.A. Patel, M. Arundell, K.H. Parker, M.S. Yeoman, D. O'Hare, Simple and rapid determination of serotonin and catecholamines in biological tissue using high-performance liquid chromatography with electrochemical detection, J. Chromatogr., B: Anal. Technol. Biomed. Life Sci. 818 (2) (Apr. 2005) 269–276, https://doi.org/10.1016/J.JCHROMB.2005.01.008.